

Magnetic torque on microfabricated elements and magnetotactic bacteria

Lars Zondervan¹, Özlem Sardan Sukas¹, Islam S. M. Khalil²,
Marc P. Pichel^{3,4}, Sarthak Misra⁴, and Leon Abelmann^{1,3}

¹*MESA⁺ Research Institute,*

University of Twente, The Netherlands

²*The German University in Cairo,*

New Cairo City, Egypt

³*KIST Europe, Saarbrücken, Germany*

⁴*MIRA, University of Twente, The Netherlands*

l.abelmann@kist-europe.de

Abstract: We present a thorough theoretical analysis of the magnetic torque on microfabricated elements with dimensions in the range of 100 to 500 μm and magneto-somes of magnetotactic bacteria of a few μm length. We derive simple equations for field dependent torque and magnetic shape anisotropy that can be readily used to replace the crude approximations commonly used. We illustrate and verify the theory on microfabricated elements and magnetotactic bacteria, by field dependent torque magnetometry and by observing their rotation in water under application of a rotating magnetic field. The maximum rotation frequency of the largest microfabricated elements agrees within error boundaries with theory. For smaller, and especially thinner, elements the measured frequencies are a factor of three to four too low. We suspect this is caused by incomplete saturation of the magnetisation in the elements, which is not incorporated in our model. The maximum rotation frequency of magnetotactic bacteria agrees with our model within error margins, which are however quite big due to the large spread in bacteria morphology. The model presented provides a solid basis for the analysis of experiments with magnetic objects in liquid, which is for instance the case in the field of medical microrobotics.

Keywords: Magnetic rotational torque, rotational drag torque, magnetotactic bacteria, SiN, Co₈₀Ni₂₀

I. INTRODUCTION

Untethered micro-robotic systems for medical applications make a compelling research field [1, 2]. It is a form of Minimally Invasive Surgery (MIS), in which one tries to reduce patient surgical trauma while enabling clinicians to reach deep seated locations within the human body [3, 4]. The current approach is to insert miniaturised tools needed for a medical procedure into the patient through a small insertion or orifice. By reducing the size of these tools a larger range of natural pathways become available. Currently, these tools are however mechanically connected to the outside world. If this connection can be removed, so that the tools become untethered, (autonomous) manoeuvring through veins and arteries of the body becomes possible [5].

If the size and/or application of these untethered systems inside the human body prohibits storage of energy for propulsion, the energy has to be harvested from the environment. One solution is the use of alternating magnetic fields [2]. This method is simple, but although impressive progress has been made, it is appallingly inefficient. Only a fraction of 10^{-12} of the supplied energy field is actually used by the microrobot.

Efficiency would increase dramatically if the micro-robot could harvest its energy from the surrounding liquid. In human blood, energy is abundant and used by all cells for respiration. Despite impressive first

attempts [6], we are however far away from using nutrient such as glucose for micro-actuation. As model systems, one could use simpler fluids to derive energy, such as peroxide [7–10]. But of course, peroxide is not compatible with medical applications.

Nature provides us however with a plentitude of self-propelling micro-organisms that derive their energy from bio-compatible liquids. There are even magnetotactic bacteria [11], that use the earth magnetic field to locate the bottom of marshes or ponds. These bacteria are perfect model systems to test concepts and study the behaviour of self-propelling micro-objects steered by external magnetic fields [12].

For self-propelled objects, only the direction of motion needs to be controlled by the external magnetic field. There is no need for field gradients to apply forces, so the field can be uniform. Compared to systems that derive their energy for propulsion from the magnetic field, the field can be small in magnitude and needs to vary only slowly. As a result, the energy requirements are low and overheating is no longer a problem.

It is generally accepted that magnetotactic bacteria react on the external magnetic field in a passive fashion, much like compass needles [13]. The direction of the motion is changed by application of a magnetic field under an angle with the easy axis of magnetisation of the micro-objects. The resulting magnetic torque causes a rotation of the micro-object at a speed that is determined by the balance between magnetic

torque and rotational drag torque.

The magnetic torque is often modelled by assuming that the magnetic element is a permanent magnet with dipole moment \mathbf{m} [Am²] on which the magnetic field \mathbf{B} [T] exerts a torque $\Gamma = \mathbf{m} \times \mathbf{B}$ [N]. This simple model suggest that the torque increases linearly with field, because it is assumed that the atomic dipoles are rigidly fixed to the lattice, and cannot rotate at all. This is usually only the case for very small magnetic fields. In general one should consider changes in magnetic energy as a function of magnetisation direction with respect to the object (magnetic anisotropy). This is correctly suggested by Erglis and co-authors for magnetotactic bacteria, but they fail to analyse the consequences [13]. Moreover, they suggest that the magnetic element of the magnetotactic bacterium (the magnetosome), can be approximated with a solid cylinder, which is a very crude approximation.

Since magnetotactic bacteria suffer from a large spread in dimensions and magnetic properties, these approximations are difficult to verify. Therefore, we have fabricated microelements of which the dimensions and magnetic properties are exactly known. We present a thorough theoretical analysis of the magnetic torque on microfabricated elements and magnetosomes of magnetotactic bacteria. We derive simple equations for field dependent torque and magnetic shape anisotropy that can be readily used to replace the crude approximations commonly used. We illustrate and verify the theory on microfabricated elements and magnetic bacteria, by torque magnetometry and by observing their rotation in water under application of a rotating magnetic field.

II. THEORY

The magnetic torque Γ [Nm] is equal to the change in total magnetic energy U [J] with changing applied field angle. Since our microfabricated elements and magnetotactic bacteria have negligible crystal anisotropy, we only consider the demagnetisation and external field energy terms. The demagnetisation energy is caused by the magnetic stray field \mathbf{H}_d [A/m] that arises due to the sample magnetisation \mathbf{M} [A/m] and is mathematically equivalent to [14]

$$U_d = \frac{1}{2} \mu_0 \int \mathbf{M} \cdot \mathbf{H}_d dV \quad (1)$$

The demagnetisation energy acts to orient the magnetisation such that the external stray field energy is minimised. We can define a shape anisotropy term K [J/m⁻³] to represent the energy difference between the hard and easy axis of magnetisation, which are perpendicular to each other

$$K = (U_{d, \max} - U_{d, \min}) / V \quad (2)$$

The external field energy is caused by the externally applied field \mathbf{H} [A/m]

$$U_H = -\mu_0 \int \mathbf{M} \cdot \mathbf{H} dV \quad (3)$$

and acts to align \mathbf{M} parallel to \mathbf{H} . Assuming that the magnetic element of volume V is uniformly magnetised with saturation magnetisation M_s [A/m], the total energy can be thus expressed as

$$U = KV \sin^2(\theta) - \mu_0 M_s H V \cos(\varphi - \theta) \quad (4)$$

The angles are defined as in figure 1a. Normalising energy, field and torque

$$u = U / KV \quad (5)$$

$$h = \mu_0 H M / 2K \quad (6)$$

$$\gamma = \Gamma / KV \quad (7)$$

the energy expression can be simplified:

$$u = \sin^2(\theta) - 2h \cos(\varphi - \theta) \quad (8)$$

The equilibrium magnetisation direction is reached for $\partial u / \partial \theta = 0$, which leads to an equation that cannot be expressed in an analytically concise form. The main results are however that for $h < 1/\sqrt{2}$, the maximum torque is reached at the field angle $\varphi_{\max} = \pi/2$,

$$\gamma_{\max} = 2h \sqrt{1 - h^2} \quad \text{for } h \leq 1/\sqrt{2} \quad (9)$$

$$= 1 \quad \text{for } h > 1/\sqrt{2} \quad (10)$$

The angle of magnetisation at maximum torque can be approximated by

$$\theta_{\max} = h + 0.1h^2 \quad \text{for } h < 1/\sqrt{2}, \quad (11)$$

where the error is smaller than 5×10^{-3} rad (1.6°) for $h < 0.5$.

For $h > 1$, the field angle φ_{\max} at which the maximum torque is reached is smaller than $\pi/2$ and approaches $\pi/4$ for $h \rightarrow \infty$. This behaviour can be very well approximated by

$$\varphi_{\max} = \frac{\pi}{4} \left(1 + \frac{2}{3h} \right) \quad \text{for } h > 1, \quad (12)$$

where the error is smaller than $3 \times 10^{-3} \pi$ (0.5°).

In summary, and returning to variables with units, the maximum torque is $\Gamma_{\max} = KV$ which is reached at

$$H > \frac{\sqrt{2}K}{\mu_0 M_s} \quad (13)$$

at an angle $\varphi = \pi/2$, which decreases in good approximation linearly with $1/H$ to $\varphi = \pi/4$ at infinite external field. In the following, we determine the value of the anisotropy energy density K for microfabricated elements as well as magnetotactic bacteria.

A. Magnetic torque of microfabricated elements

The microfabricated elements are thin film rectangular elements. We can calculate the magnetic torque either for field applied perpendicular or in the film plane.

1. Perpendicular fields

The microfabricated elements have lateral dimensions much larger than the film thickness. Therefore, the demagnetisation field strength is zero for fields applied in the film plane and equal to M if the field is directed perpendicular to the film plane. The maximum demagnetisation energy difference for fields applied in a plane perpendicular to the film plane (figure 1a), is simply

$$KV = \Gamma_{\perp\max} = \frac{1}{2}\mu_0 M_s^2 V \quad (14)$$

2. In-plane fields

For fields applied in the thin film plane, the shape energy term is more complex. If again we assume that the external field is sufficiently high, so that the magnetisation aligns with the field, the maximum torque is determined by the difference in magnetic energy for the field aligned along either edge of the film.

Since there are no free currents, we can define a magnetic scalar potential ϕ and consider magnetic charges [15]. For in-plane magnetisation the charges are located at the film edges. If the film thickness t is much smaller than the lateral dimensions L and W , we can approximate the charge densities by line charges $\lambda = M_s t$ [A]. The energy of such a line charge in the magnetic field potential of the opposite line charge is

$$U = \frac{1}{2}\mu_0 \int \lambda\phi dl, \quad (15)$$

where the integral is taken along the line. For a magnetisation along the x direction, as shown in figure 2, the magnetic potential can be calculated by a summation of the potential of individual point charges:

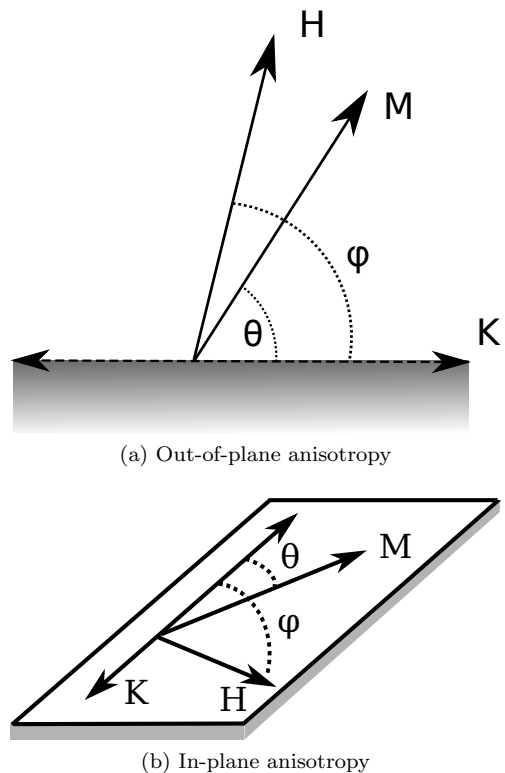


FIG. 1: Definition of the field angle φ and the magnetisation angle θ between the easy axis K of the thin film, the magnetization M and the magnetic field H for (a) out-of-plane and (b) in-plane anisotropy.

$$\phi_{\pm}(x, y) = \pm \frac{\lambda}{4\pi} \int_{-L/2}^{L/2} \frac{1}{r_{\pm}(y')} dy' \quad (16)$$

where the line charges are located at $x = \pm \frac{W}{2}$. Rewriting r in terms of (x, y) and solving the integral we obtain

$$\phi_{\pm}(x, y) = \pm \frac{\mu_0}{4\pi} \ln \left(\frac{(y - L/2)\sqrt{(y - L/2)^2 + (x + W/2)^2}}{(y + L/2)\sqrt{(y + L/2)^2 + (x - W/2)^2}} \right) \quad (17)$$

Taking the reference potential at $(0,0)$ for both ϕ_+ and ϕ_- , and solving integral (15), we obtain for the magnetic energy for a field along x

$$U_x = \frac{\lambda^2 \mu_0}{2\pi} \left(W - \sqrt{L^2 + W^2} \right) \quad (18)$$

The energy for a field applied along y , U_y , can simply be obtained by reversing W and L , and we obtain for the energy difference $U_x - U_y$, and therefore the maximum in-plane torque,

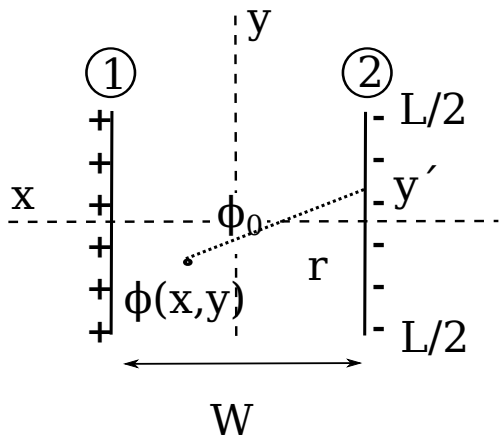


FIG. 2: Charged line approximation of an in-plane thin film magnetised along its width W .

$$\Gamma_{\parallel\max} = \frac{\lambda^2 \mu_0}{2\pi} (W - L) \quad (19)$$

As expected, the maximum torque is zero for a square element.

After replacing λ with $M_s t$, we can compare the in-plane and perpendicular torque:

$$\Gamma_{\parallel\max} = \Gamma_{\perp\max} \left(\frac{W - L}{W} \right) \frac{t}{L\pi} \quad (20)$$

Since $t \ll L$ (and W), the in-plane torque is much smaller than the perpendicular torque. For the elements we designed (table I), the maximum ratio is at most 2.4×10^{-3} , so the out of plane demagnetisation factor is to a very good approximation equal to unity. Therefore the in-plane difference in demagnetisation factors can be determined from

$$\Delta N = \left(\frac{W - L}{W} \right) \frac{t}{L\pi}, \quad (21)$$

and the field dependent torque becomes

$$\Gamma = \Gamma_{\parallel\max} 2h \sqrt{1 - h^2} \quad (22)$$

$$h = \frac{H}{\Delta N M_s}. \quad (23)$$

For the 2.5 mT field applied in our experiments, $h < 1/\sqrt{2}$ for all elements and the maximum torque is not attained.

B. Magnetic torque of magnetotactic bacteria

In contrast to the microfabricated elements, the magnetosome of magnetotactic bacteria is less well

defined. As a first approximation, we can consider the chain of magnetic spheres as a chain of n dipoles separated at distance a , each with a dipole moment $m = M_s V$ [Am²], where V is the volume of each single sphere. Again, we assume that all dipoles are aligned parallel to the field ($\varphi = \theta$) to obtain an upper limit on the torque. (See figure 1 for angle definition). The magnetic energy for such a dipole chain has been derived by Jacobs and Bean [16], which rewritten in SI units is

$$U = \frac{\mu_0 m^2}{4\pi a^3} n K_n (1 - 3 \cos^2(\theta)) + \mu_0 n m H \cos(\varphi - \theta) \quad (24)$$

$$K_n = \sum_{j=1}^n \frac{(n-j)}{n j^3} \quad (25)$$

The maximum torque equals the energy difference between the state where all moments are parallel to the chain ($\theta=0$) and the state where they are perpendicular to the chain ($\theta=\pi/2$):

$$\Gamma_{\max} = \frac{1}{2} \mu_0 M_s^2 n V \Delta N \quad (26)$$

$$\Delta N = N_{\perp} - N_{\parallel} = \frac{1}{4} K_n. \quad (27)$$

As expected, for a single dipole, $n = 1$ and there is no energy difference. The expression for the field dependence of the torque is equal to that of the microfabricated elements (equation 22).

The magnetosome does not consist of point dipoles but should be approximated by spheres with radius r , spaced at distance d from each other (figure 3). Naively, we could simply modify the Jacob and Bean model by setting

$$a = \frac{d}{r} + 2, \quad (28)$$

leading to

$$\Delta N = \frac{2K_n}{\left(\frac{d}{r} + 2\right)^3} \quad (29)$$

as a correction of equation 27. It is not immediately clear that this naive correction is valid. Intuitively, one could assume that the field of a uniformly magnetised sphere is identical to a dipole field. We ignore however that the field of neighbouring dipoles is not uniform over the volume of the sphere. To investigate this effect, we performed finite element simulations.

1. FEM calculations

Since there are no free currents, $\nabla \times \mathbf{H} = 0$ and the magnetic field can be expressed by a scalar magnetic

potential field $\mathbf{H} = -\nabla\phi$ [A/m] and accompanying magnetic charge $\nabla \cdot \mathbf{H} = \rho = -\nabla \cdot \mathbf{M}$ [A/m²]. The partial differential equation to be solved in a cylindrical coordinate system then becomes

$$x \frac{\partial^2 \phi(x, y)}{\partial x^2} + x \frac{\partial^2 \phi(x, y)}{\partial y^2} = \rho(x, y). \quad (30)$$

where x is the radial coordinate and y is along the axis. This differential equation was solved in FreeFEM++ [17], see for example figure 4. We assume a uniform magnetisation along the axis of the chain of spheres, which leads to a sinusoidal magnetic surface charge distribution on each semi circular boundary ($\sigma = \mathbf{M} \cdot \mathbf{n}$ [A/m]). Integrating $\mathbf{m} \times \mathbf{H}$ over the surface of each semi circle times 2π (as a cylindrical coordinate system is used), the demagnetisation energy of the magnetic chain is acquired. By dividing the demagnetisation energy by the summed volume of all spheres in the chain the demagnetisation factor for fields applied along the axis of the chain (N_{\parallel}) is found. Since the system is cylindrically symmetric and the sum of the demagnetisation factors equals unity, $N_{\parallel} + 2N_{\perp} = 1$, so

$$\Delta N = \frac{1}{2} (1 - 3N_{\parallel}). \quad (31)$$

To obtain generic results, the dimensions were scaled to r and potential to ρ . Numerical calculations were performed with varying mesh densities of 6, 10, 14 and 18 points per unit length. The final value for the demagnetisation factor is obtained by extrapolating to infinite mesh densities. The distance C from the first and last sphere of the chain to the boundary is varied and chosen such that no significant effect of the boundary on the simulation results is observed. Under these conditions, the numerical calculation was found to be accurate within 0.1% for the demagnetisation factor of a single sphere ($\frac{1}{3}$).

To find the demagnetisation energy of an infinite chain of spheres, one semi circle in a rectangular geometry is defined, see figure 5, with periodic boundary conditions on the top and bottom boundaries of the rectangle. This creates an infinite chain of spheres with radius $r=1$, spaced d apart. The periodic boundary ensures that the field, which is leaving the simulation space from the top, enters the simulation space from the bottom, and vice versa. The demagnetisation energy is found in a similar manner as for the FEM calculation of n spheres spaced d apart.

The value of ΔN obtained from the numerical calculations is shown in figure 6, together with the naive correction to the Jacobson and Bean chain of spheres model. The number of spheres n was varied from 2 to ∞ , and sphere spacing d/r was varied from 0 to 10. For demagnetisation factors > 0.01 the chain of

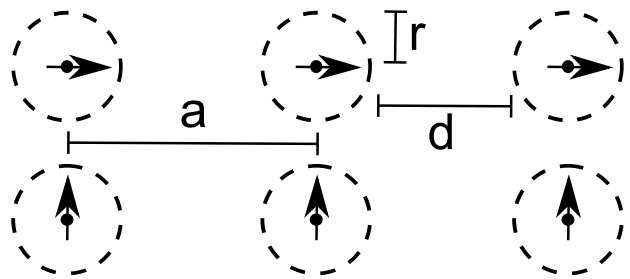


FIG. 3: Chain of magnetic spheres of radius r , spaced by distance d , approximated by point dipoles spaced by a distance $a = r + d$, magnetised along the longitudinal axis of the chain (top) or perpendicular to its longitudinal axis (bottom).

spheres model agrees within 3% with the outcome of numerical calculation. The increase in deviation at smaller demagnetisation factors is due to numerical errors in the FEM calculation.

We therefore conclude that the chain of spheres model provides a very good, if not exact, solution. It is therefore safe to use equation 29 in the calculation of the magnetic torque (eq 26) on a magnetism.

For an infinitely long chain of touching spheres, $d=0$ and $n \rightarrow \infty$, the difference in demagnetisation factors ($N_{\perp} - N_{\parallel}$) approaches 0.3. Approximating the chain with a long cylinder ($N_{\perp} - N_{\parallel}=0.5$) [13, 18], overestimates the maximum torque by 40%. Simply taking the total magnetic moment to calculate the torque, as if $N_{\perp} - N_{\parallel}=1$, would overestimate by a factor of three.

The FEM calculation shows a property of magnetostatic fields of spherical objects that was unknown to the authors. Apparently interaction energy between two uniformly magnetised spheres can be simplified by mere dipole interaction, leading to the collapse of a six-fold integral into a simple product. This is very similar to the center of mass concept in gravitational and electrostatic interaction.

C. Rotational Drag torque

The torque exerted by the magnetic field results in the rotation of the microfabricated elements or magnetotactic bacteria. This rotation on its turn causes a counter torque, which increases with increasing rotational velocity. An equilibrium steady state velocity is obtained when the magnetic torque is balanced by the drag torque. Since we work with very low mass objects, this steady state is reached almost immediately in comparison to the duration of the experiment. In the following we will discuss the drag torque for mag-

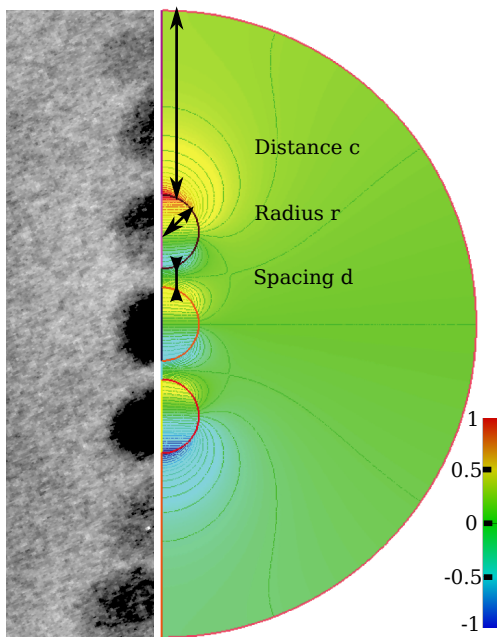


FIG. 4: FEM results of n magnetic spheres spaced distance d apart at distance c from the edge of the simulation area. In this case $n=3$, $r=1$, $d/r=0.2$ and $c/r=5$ (chosen for convenient display). The color code and contour lines indicate the magnetic scalar potential [A] using a sphere magnetisation of 1 A/m.

On the left, part of the TEM image of figure 9 illustrates the magnetosome.

netotactic bacteria and microfabricated elements, as well as the resulting rotational velocity.

1. Magnetotactic bacteria

magnetotactic bacteria are very small, and rotate at a few revolutions per second only. Inertial forces therefore do not play a significant role. The ratio between viscous and inertial forces is characterised by the Reynolds number R , which for rotation at angular velocity ω [rad/s] is

$$R = \frac{L^2 \rho \omega}{4\eta}, \quad (32)$$

where L is the characteristic length (in our case the length of the bacterium), ρ the density and η dynamic viscosity of the liquid (for water respectively 10^3 kg/m³, and 1 mPas). Experiments by Dennis *et al* [19] show that a Stokes flow approximation for the drag torque is accurate up to $R=10$. In experiments with bacteria, the Reynolds number is the order of 10^{-3} and Stokes flow approximation is certainly allowed. The drag torque is therefore

$$\Gamma_D = f_r \omega, \quad (33)$$

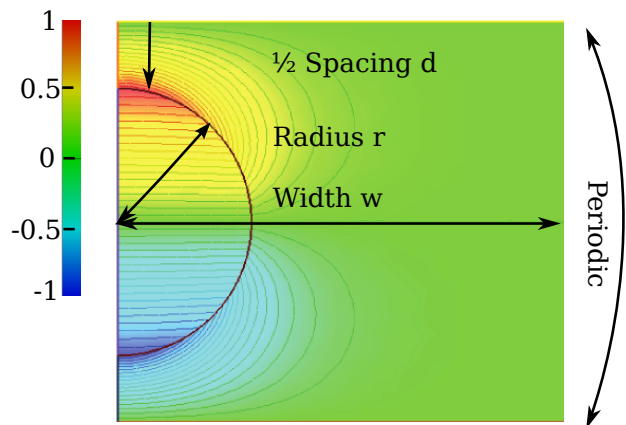


FIG. 5: FEM results of an infinite chain of spheres spaced distance d apart. The top and bottom side of the cylindrically symmetric, rectangular simulation domain are periodic boundaries. In this case $d/r=1$ (of which only half falls in the simulation space), $w/r=2.5$ (chosen small for convenient display).

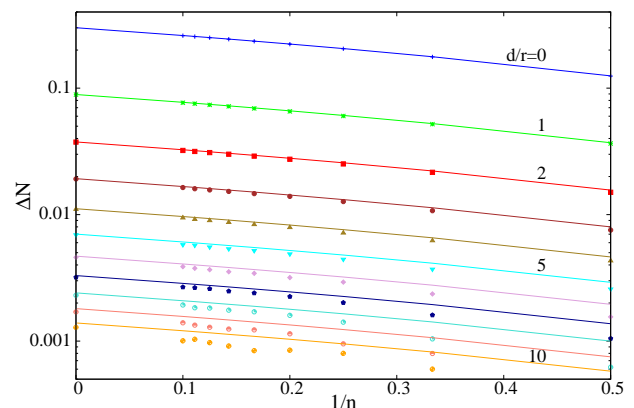


FIG. 6: Difference in demagnetisation factors of a chain of spheres as function of number of spheres n for varying spacing between the spheres d/r . Shown are FEM calculations (symbols) and the Jacobs and Bean model (lines).

where the drag coefficient f_r can be approximated by

$$f_r = \frac{\pi \eta L^3}{3 \ln \left(\frac{2L}{W} \right) - \frac{3}{2}} \quad (34)$$

assuming that the bacterium is a prolate spheroid with length L and diameter W [20].

2. Microfabricated elements

In principle, one could fabricate elements using lithographic techniques of identical size to magnetotactic bacteria. The handling of such elements will

be however be cumbersome, since one cannot use tweezers at that scale. When scaling up however, we should remain in the Stokes flow regime for the viscous drag model to remain valid. Therefore we increased the size of the elements up to the point that their Reynolds number equals approximately unity, well below 10 so that Stokes flow approximations can still be assumed.

We approximate the rectangular elements with a disc of diameter equal to the length of the element L [20]. Since the elements are floating on the water surface, we further assume that we can simply divide the drag coefficient by two, since drag will only occur on one side of the element. Under these assumptions, the drag coefficient is

$$f_r = \frac{1}{2} \left[\frac{32}{3} \eta \left(\frac{L}{2} \right)^3 \right] = \frac{2}{3} \eta L^3. \quad (35)$$

The assumptions are rather crude, but not significant compared to measurement errors.

D. Maximum rotation frequency

Finally, the maximum steady-state rotational speed will be obtained when the maximum magnetic torque equals the rotational drag torque

$$\omega_{\max} = \frac{\Gamma}{f_r} \quad (36)$$

III. EXPERIMENTAL

A. Microfabrication

The microfabricated elements are realised by surface micro machining techniques on a 100 mm diameter p-type silicon wafer (orientation $\langle 100 \rangle$). The fabrication steps are illustrated in figure 7. A four mask process is used with masks numbered I to IV.

Fabrication starts with the deposition of 2-3 μm low-stress nitride in a LPCVD process (step (A)). Next, a photoresist mask is patterned using Mask I and the unprotected nitride is removed with RIE using a plasma of CHF_3 and O_2 . The excess resist is removed in a oxygen plasma (B). A new layer of photoresist is patterned using Mask II after which a 200 nm thick $\text{Co}_{80}\text{Ni}_{20}$ layer is deposited using e-beam evaporation to define the magnetic strips. A lift-off process (C) is used to remove the excess metal and photoresist. Using Mask III a new layer of photoresist is patterned and after sputtering 75 nm Pt a similar lift-off process is used (D). This lift-off procedure is repeated using Mask IV after sputtering a

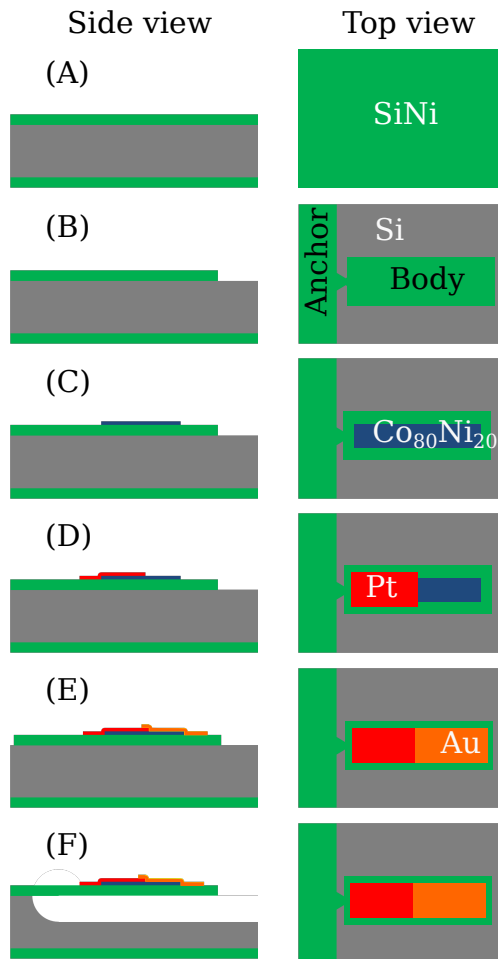


FIG. 7: Side view (left) and top view (right) of the process flow used to fabricate silicon-nitride elements with a magnetic strip. See text for a description of the process steps.

75 nm Au layer (E). The Pt/Au structures were intended for experiments with self-propelled structures in peroxide solution [7], which failed however and are not reported in this paper. Using Mask I again a protective layer of photoresist is patterned to protect the nitride/metal structures during XeF_2 etching of silicon (at 530 Pa pressure). Finally the photoresist is removed using O_2 plasma etching (F). The free hanging nitride structures with metal layers on top are still anchored to the substrate but can be easily snapped off using tweezers or a needle (Figure 8).

Table I lists the dimensions of the nitride supports (W, L) and their magnetic strips (w, l) for the elements used in the rotation experiments. Table II list the array of elements that was used for the torque magnetometry experiments.

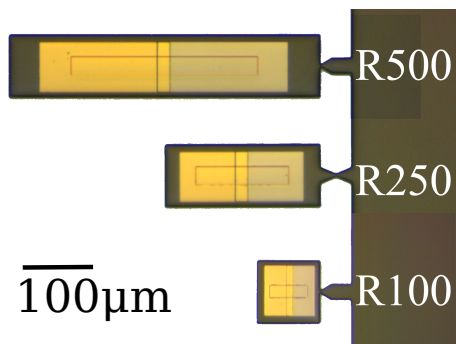


FIG. 8: Three rectangular elements of different length (500, 250 and 100 $\mu\text{m} \times 100 \mu\text{m}$), still attached to their support. These elements are broken off by a tweezer and placed on the water surface.

TABLE I: Microelements design (width and length of silicon-nitride elements (W, L) and magnetic elements (w, l)), drag coefficient f_r , maximum torque $\Gamma_{\parallel\text{max}}$, effective field h and torque Γ_{\parallel} for a field of 2.5 mT

W	L	w	l	f_r	$\Gamma_{\parallel\text{max}}$	h	Γ_{\parallel}
[μm]	[μm]	[μm]	[μm]	[fNm/s]	[pNm]		[pNm]
25	100	5	60	0.7	0.6	0.14	0.09
25	250	5	150	10	1.6	0.14	0.22
25	500	5	300	83	3.3	0.13	0.44
50	100	15	60	0.7	0.5	0.52	0.23
50	250	15	150	10	1.5	0.44	0.60
50	500	15	300	83	3.2	0.41	1.21

B. Growth of magnetotactic bacteria

The magnetotactic bacteria used were *Magnetospirillum magnetotacticum*, MS-1, isolated by ATCC (31632), purchased through LGstandards and delivered on dry ice. The growth medium is prepared using the instructions from ATCC in accordance with [21] and [11]. The frozen culture is placed in the growth medium and left to defrost in an 16 mm \times 125 mm vial, kept at 27 $^{\circ}\text{C}$. The bacteria are harvested after an incubation period of two weeks by centrifuging the sample at 7000 rpm and discarding the supernatant liquid. Part of the harvested MTB

TABLE II: Elements in array measured by TMM

Amount	Area nitride [μm]	Area $\text{Co}_{80}\text{Ni}_{20}$ [μm]
68	500 \times 100	300 \times 30
68	250 \times 100	150 \times 30
34	100 \times 100	60 \times 30

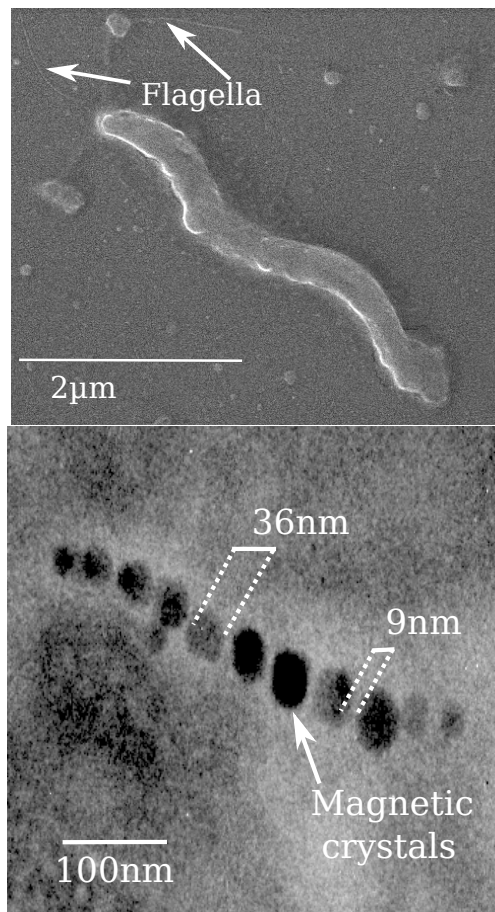


FIG. 9: Top: SEM image of a magnetotactic bacterium. The flagellae can be observed at the top left. Bottom: TEM image of the magnetosome chain.

are suspended on new growth medium for future use.

The magnetotactic bacteria were observed in a Scanning Electron Microscope (SEM, JEOL 6510) and a Transmission Electron Microscope (TEM, Gatan / FEI EFTEM). Figure 9 shows a SEM image of a single magnetotactic bacterium with its flagella, as well as a TEM image of the magnetosome chain.

C. Torque magnetometry

After fabrication, the microfabricated elements are still anchored to the substrate and torque magnetometry measurements can be performed. Since the torque of individual elements is far below the sensitivity of the magnetometer, measurements were done on an array (table II). But even on an array of over 100 elements the in-plane torque is too small to be detected. Therefore we only investigated the torque for the magnetic field rotating out of the film plane.

Torque magnetometry was performed on a home-

built instrument which measures the torque on a sample of magnetic material as a function of the magnitude and angle of the external magnetic field. The sample is attached to a glass rod suspended from a thin torsion wire and subjected to a uniform magnetic field generated by an electromagnet that can be rotated around the sample. Rather than measuring the rotation of the glass rod, the torque applied to the sample by the electromagnet is compensated by a counteracting torque. For this a feedback coil is attached to the glass rod, which is placed in the field of two small permanent magnets. The rotation of the glass rod is measured by a light beam reflected on a mirror on the glass rod towards two side-by-side placed photo diodes. The current through the feedback coil is adjusted such as to keep the focused light beam exactly between the photo diodes. This current is logged and, once calibrated, is an accurate measure of the magnetic torque exerted on the sample. In this way, any variation in the torsional spring constant of the suspending wire are eliminated.

D. Optical microscopy

Experiments with the microfabricated elements and bacteria were performed in a microscope equipped with a video acquisition system and a set of coils to generate magnetic fields. Opposite coils are connected in series, and driven with sinusoidal currents with a 90° phase difference between the orthogonal coil sets. This generates a uniform, rotating magnetic field.

For the microfabricated elements, a small container was fabricated by 3D printing, which could be positioned under the microscope objective and between the coil system, see figure 10. The microfabricated elements were broken out of the support wafer with a tweezer and positioned on the water surface. Forcefully submerging the elements was possible, in which case the elements sank to the bottom of the container. In that case however the elements stuck to the container surface and could not be rotated. A rotating magnetic field of 2.5 mT was applied and its frequency was slowly increased. The frequency at which the elements stopped following the field and started wobbling was recorded. The experiment was repeated five times per element.

Experiments on the bacteria are conducted using borosilicate capillaries (VitroCom, VitroTubes 3520-050, Germany) with a rectangle channel of $0.2 \text{ mm} \times 2 \text{ mm}$ and a length of 50 mm. The capillaries are filled with growth medium containing magnetotactic bacteria and the ends of the capillary are sealed with parafilm. The circular motion (superposition linear movement due to flagella propulsion and rotary movement due to magnetic torque) of the bacteria was captured for varying rotation magnetic field

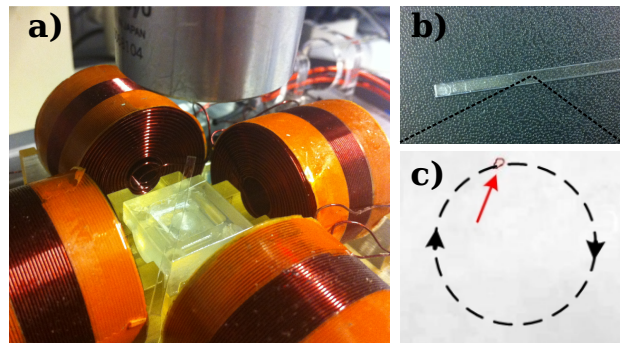


FIG. 10: Measurement setup. a) Four coils are used to generate an in-plane magnetic field of arbitrary direction b) The magnetotactic bacteria are inserted in a cuvette c) A microscope with video-capture system and tracking software is used to monitor the movement of the bacteria.

frequencies.

IV. RESULTS AND DISCUSSION

A. Torque measurements on microfabricated elements

Figure 11 shows the magnetic torque as a function of applied field angle, where the field is rotating in a plane perpendicular to the sample surface and parallel to the long axis of the elements. The signal is at the limit of the instruments capability, but the torque clearly increases with increasing field value. At low fields, some hysteresis is visible which indicates that in zero field the magnetic elements most likely have a remanent magnetisation.

By averaging, an accurate estimate of the maximum torque can be obtained, which is plotted as a function of the external field in figure 12. Also shown is the theoretical prediction of the field dependent torque (section II A 1), based on the designed lateral dimensions of the elements, the magnetic layer thickness obtained from the deposition run and assuming that the composition of the Co-Ni film is exactly 80/20 which leads to a saturation magnetisation of 1.19 MA/m. No fit parameter has been applied. Considering that the layer thickness has an estimated error of 5%, the agreement between model and experiment is excellent.

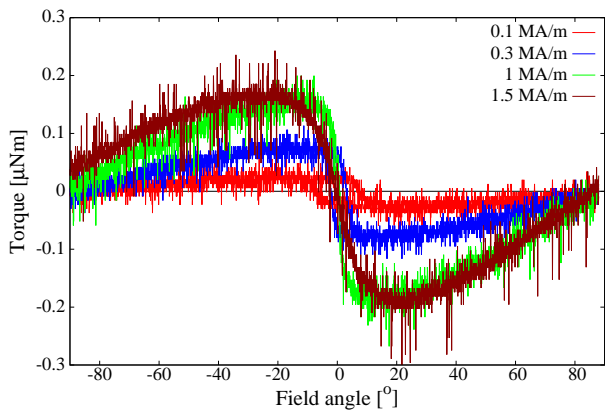


FIG. 11: Measured out-of-plane torque curves as a function of the field angle for varying magnetic field strength.

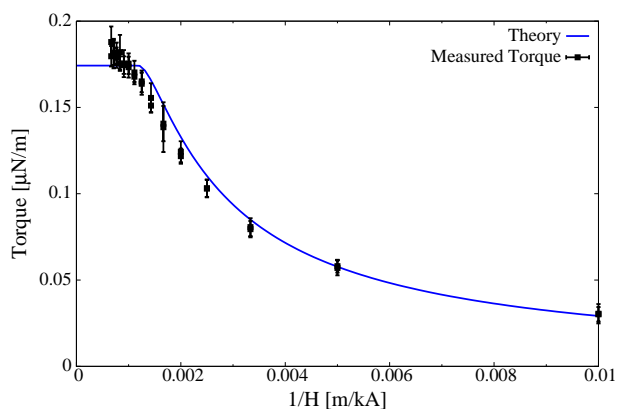


FIG. 12: Measured maximum out-of-plane torque as a function of magnetic field strength compared to the modeled expected behaviour (solid line), which does not include any fit parameter.

B. Maximum rotation frequency of microfabricated elements

Figure 13 shows the maximum rotation frequency for the elements listed in table I, sorted by the length of the object. Also shown is the theoretical prediction, using drag coefficient and magnetic torque as listed in table I. Since the dimensions of the magnetic elements is varying with object length, the theoretical maximum rotation frequency is only calculated for specific elements, and connected by a line to guide the eye.

For all measurements, the observed maximum rotation frequency lies below the theoretical prediction. This can only partly be explained by the measurement procedure, in which the maximum frequency is

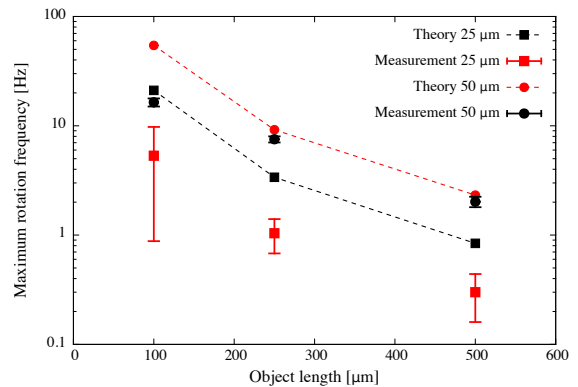


FIG. 13: Maximum rotation frequency as a function of object length for rectangles of 25 (red squares) and 50 μm (black circles) width. (Model points are connected by a line to guide the eye, see table I).

approached from below. The difference between the 25 and 50 μm elements is however pronounced. The 50 μm elements show small scatter between experiments, and for the larger element the difference with theory is small. The 25 μm elements however show much more scatter, and differ from theory by a approximately a factor of three.

The difference between the two series is probably not caused by a difference in drag, which is dominated by the length of the element. The 25 μm elements however have magnetic strips with a much smaller width, leading to higher saturation fields and relatively low effective fields (h in table I). We speculate that the assumption of uniform magnetisation might not hold for fields that only 15% of saturation field. Comparing with fields applied out of the plane, we indeed observe hysteresis effects for fields below 300 kA/m, which is 25% of the saturation field. It is possible that the magnetisation in the strip splits up in domains, leading to a reduction in torque and increase in scatter due to hysteresis effects. The electromagnet in our setup was unfortunately not capable of generating higher rotating fields, so this hypothesis could not be verified.

C. Maximum torque of magnetotactic bacteria

Figure 14 shows a typical trajectory of a magnetotactic bacterium under application of a rotating magnetic field. In the sequence of images, the frequency of rotation is increased at constant rate until the bacteria no longer follows the field. In this way we estimate that that maximum rotation frequency lies in the range of 7 to 10 rad/s.

From SEM and TEM images of fifteen magnetotactic bacteria (figure 9), we determined their dimen-

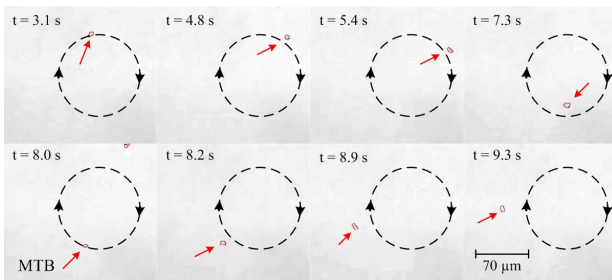


FIG. 14: Motion of a magnetotactic bacterium under the influence of a rotating magnetic field of 7.9 mT with gradually increasing frequency from 1 to 10 rad/s. The black-dashed circle illustrates the path and direction of the bacterium (red arrow). The images are processed to detect the edges of the bacterium. As we gradually increase the rotating field frequency to 9.5 rad/s, the bacterium can no longer follow the field. (Reprinted with permission from [23])

sions and the size, spacing and number of crystals in the magnetosomes. The minimum, maximum and average values are listed in table III. Applying the chain-of-spheres model to the magnetosome data results in ΔN values of 0.07 to 0.13. As a result torque values ranging from 0.02 to 4 aNm, with an average of about 1 aNm at 7.9 mT.

For the calculation of the field dependent torque, we assume that the magnetisation of the crystals is that of bulk magnetite (Fe_3O_4 , 480 kA/m [22]). Using this value our model predicts that at 7.9 mT the torque has not yet saturated, and could for average bacteria be increased by a factor five if the field were increased to $h = 1/\sqrt{2}$, so $B=59$ mT. At 7.9 mT, the field is still sufficiently low allow approximation of the torque by $\mathbf{m} \times \mathbf{B}$, with an error of less than 2%. The error however increases to at least 50% at the field at which maximum torque is reached, and keeps on increasing.

Unfortunately, the SEM and TEM images could not be performed on identical bacteria. For the calculation of their theoretical maximum rotation frequency, we assumed however that the dimensions of the bacteria and their magnetosomes are correlated. In that case we predict maximum rotation frequencies to range from 8 to 66 rad/s with an average of 20. Our observation rotation frequency of 10 rad/s lies within that range.

V. DISCUSSION AND OUTLOOK

Using electromagnetic coil systems, it is difficult to achieve high field values. As a result, our experi-

mental setup did not allow us to reach the maximum torque that could in principle be applied to both the microfabricated elements and magnetotactic bacteria. The theory in section II provides a simple expression for field dependent torque, which is verified by the out-of-plane torque measurements of figure 12. This provides a proven and simple framework to design future experiments.

Our experiments show that too low field values cause irreproducible results and large deviations from our analytical model. Incorporation of domain theory into the model will make it far less useable. It is therefore advisable to design magnetic field systems that are capable of higher field values, for instance by using permanent magnet systems that can mechanically be adjusted to tune field direction and strength. For magnetotactic bacteria, field values should exceed 60 mT.

Correct analysis of the experiments with the microfabricated elements suffered from the fact that they had to be floated on the water surface. When submerged however, the elements sink to the bottom, which again will complicate modelling. Unless one finds a way to levitate the elements, the influence of interfaces has to be incorporated in the model. For future experiments, it would be advisable to carefully take the interface into account. One could for instance position the elements at the interface between water and oil, which will provide a more reproducible situation.

The FEM simulations show that the simple, analytical *chain of spheres* model accurately predicts the maximum magnetic torque on a magnetosome. There is no need to approximate the magnetosome with a solid cylinder, or even worse, a single dipole.

The SEM and TEM observations show that there is a large spread in dimensions and magnetic properties within a colony of magnetotactic bacteria. Experimental difficulty prohibits correlation between the size of a bacterium and its maximum magnetic torque. In future experiments, it would be advisable to expand the number of measurements to determine distributions, or to pre-filter bacteria on a certain property such as for instance size, speed or minimum radius of curvature.

Based the extreme values of table III, we can estimate the field dependence of the torque of magnetotactic bacteria using the theory of section II. For convenience, the field dependence of the torque, normalized to the maximum torque $\Gamma_{\parallel\text{max}}$, is plotted in figure 15. Also shown is the approximation for the case when the magnetisation remains aligned with the easy axes, $\Gamma_{\parallel} = \mathbf{m} \times \mathbf{B}$, which is valid up to fields of about 10 mT.

TABLE III: Minimum, mean and maximum characteristics of magnetotactic bacteria. Length L and width W and amount n , radius r and spacing d of magnetosomes. From these values the drag coefficient f_r , demagnetisation factors ΔN , magnetic moment m and maximum magnetic torque $\Gamma_{\parallel\text{max}}$ are estimated. For a field of 7.9 mT, the effective field h , torque Γ_{\parallel} and resulting rotation frequency ω are calculated.

	L	W	n	r	d	f_r	ΔN	m	$\Gamma_{\parallel\text{max}}$	h	Γ_{\parallel}	ω
	[μm]	[μm]	[#]	[nm]	[nm]	[zNs]		[aAm ²]	[aNm]		[aNm]	[rad/s]
min	2	0.10	6	6	6	2.6	0.07	2.61	0.05	0.19	0.02	7.7
mean	5	0.20	10	17	9	38	0.13	98.8	3.8	0.10	0.77	20
max	6	0.25	16	26	15	67	0.13	566	22	0.10	4.4	66

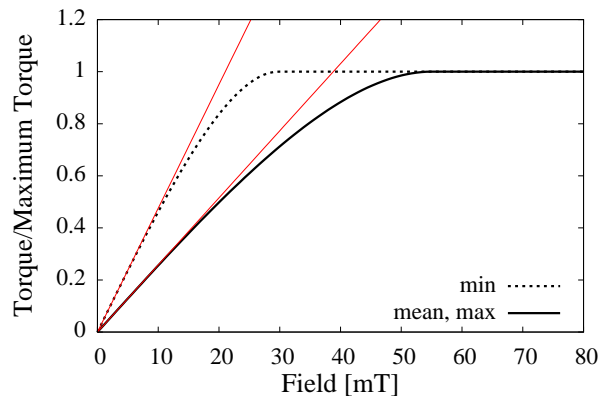


FIG. 15: Torque on magneto-tactic bacteria, normalized to the maximum torque, as a function of applied field for the smallest bacterium in table III (min) and the largest (max). Since ΔN for an average bacterium is almost equal to that of the largest bacterium, its curve overlaps with the curve for the largest bacterium. The red solid asymptotes show the approximation for $\Gamma_{\parallel} = \mathbf{m} \times \mathbf{B}$.

VI. CONCLUSION

We have modelled and measured the magnetic torque and maximum rotation frequency of microfabricated elements with dimensions in range of 100 to 500 μm , as well as magnetotactic bacteria that have a length of a few μm .

Using torque magnetometry we were able to measure the torque of an array of 170 microfabricated elements as a function of applied field angle, but only for fields applied out of the film plane. The maximum out-of-plane torque is reached at fields of about 1.2 T, and agrees within measurement errors with our model. For a single element the out-of-plane torque is in the order of 1 nNm. We calculate the in-plane torque to be in the order of 1 pNm, which is below the sensitivity of our torque magnetometer, even in a large array.

The maximum rotation speed of microfabricated

elements and magnetotactic bacteria under application of a rotating external field was measured. For microfabricated elements, the maximum rotation frequency drops with the length of the element. For our 50 μm wide microfabricated elements, we find maximum rotation speeds in the order 10 rad/s, which agrees within error boundaries with our model based on the competition between magnetic and drag torque for elements of 250 and 500 μm length. For elements of 100 μm and all 25 μm wide elements however, the measured maximum rotation frequency is a factor of three to four lower than predicted by this model. We suspect that this is caused by incomplete saturation of the magnetisation in the elements.

By means of finite elements simulations, we show that the maximum magnetic torque on the magnetosome chain can be accurately calculated by an analytic *chain of spheres* model. From TEM images of the magnetosomes, we calculate the average maximum magnetic torque to be about 1 aNm. The values range between 0.02 and 4.4 aNm, due to the large spread in bacteria morphology.

Using average bacteria dimensions measured by SEM, combined with the maximum torque determined from TEM image, we calculate an average maximum rotation frequency of 20 rad/s, with values ranging from 8 to 66 rad/s. The maximum measured angular velocity of magnetotactic bacteria in a rotating magnetic field is in the order of 10 rad/s, which is in fair agreement with our model.

Summarising, our experiments show that a simple model based on magnetic torque and viscous drag describes the maximum rotation velocity for microfabricated elements for two out of six investigated combinations of outer dimensions and magnetic element sizes within measurement accuracy, but overestimates this value by at most a factor of three for the others. Application of this model to magnetotactic bacteria leads to predictions of maximum rotation frequencies which are in agreement with observations. In the first place, this confirms the assumption that magnetotactic bacteria act passively on the external magnetic field, like compass needles. Secondly, the theory developed in this paper will support the analysis of experiments with magnetic objects in liquid, which is for instance the case in the field of medical microrobotics.

Acknowledgments

The authors wish to acknowledge the contribution of Hans Kolk, who did a major part of the measurements during his bachelor study. We are grateful for

the contribution of Remco Sanders in the preparation of magnetotactic bacteria and follow up experiments, Thijs Bolhuis for magnetic characterization and Jasper Keuning for setting up and performing initial experiments and programming of the image recognition software. This work was partially funded by the MIRA Research Institute of the University of Twente.

-
- [1] A. Menciassi, M. Quirini, and P. Dario, *Minimally Invasive Therapy & Allied Technologies* **16**, 91 (2007).
- [2] J. J. Abbott, M. Cosentino Lagomarsino, L. Zhang, L. Dong, and B. J. Nelson, *The International Journal of Robotics Research* (2009), doi:[10.1177/0278364909341658](https://doi.org/10.1177/0278364909341658).
- [3] H. Nelson, D. Sargent, H. Wieand, J. Fleshman, M. Anvari, S. Stryker, R. Beart Jr., M. Hellinger, R. Flanagan Jr., W. Peters, et al., *New England Journal of Medicine* **350**, 2050 (2004), doi:[10.1056/NEJMoa032651](https://doi.org/10.1056/NEJMoa032651).
- [4] M. Abayazid, R. J. Roesthuis, R. Reilink, and S. Misra, *IEEE transactions on robotics* **29**, 542 (2013).
- [5] J. Dankelman, J. van den Dobbelsteen, and P. Breedveld, in *Instrumentation Control and Automation (ICA), 2011 2nd International Conference on* (2011), pp. 12–15, doi:[10.1109/ICA.2011.6130118](https://doi.org/10.1109/ICA.2011.6130118).
- [6] M. Pilarek, P. Neubauer, and U. Marx, *Sensors and Actuators, B: Chemical* **156**, 517 (2011), doi:[10.1016/j.snb.2011.02.014](https://doi.org/10.1016/j.snb.2011.02.014).
- [7] R. Ismagilov, A. Schwartz, N. Bowden, and G. Whitesides, *Angewandte Chemie - International Edition* **41**, 652 (2002), doi:[10.1002/1521-3773\(20020215\)41:4<652::AID-ANIE652>3.0.CO;2-U](https://doi.org/10.1002/1521-3773(20020215)41:4<652::AID-ANIE652>3.0.CO;2-U).
- [8] S. Fournier-Bidoz, A. Arsenault, I. Manners, and G. Ozin, *Chemical Communications* pp. 441–443 (2005), doi:[10.1039/b414896g](https://doi.org/10.1039/b414896g).
- [9] S. Sundararajan, P. E. Lammert, A. W. Zudans, V. H. Crespi, and A. Sen, *Nano Letters* **8**, 1271 (2008), doi:[10.1021/nl072275j](https://doi.org/10.1021/nl072275j).
- [10] A. A. Solovev, W. Xi, D. H. Gracias, S. M. Harazim, C. Deneke, S. Sanchez, and O. G. Schmidt, *ACS Nano* **6**, 1751 (2012), doi:[10.1021/nn204762w](https://doi.org/10.1021/nn204762w).
- [11] R. P. Blakemore, D. Maratea, and R. S. Wolfe, *Journal of Bacteriology* **140**, 720 (1979).
- [12] I. S. M. Khalil, M. P. Pichel, L. Abelmann, and S. Misra, *The International Journal of Robotics Research* **32**, 637 (2013), doi:[http://dx.doi.org/10.1177/0278364913479412](https://doi.org/http://dx.doi.org/10.1177/0278364913479412).
- [13] K. Erglis, Q. Wen, V. Ose, A. Zeltins, A. Sharipo, P. A. Janmey, and A. Cebers, *Biophysical Journal* **93**, 1402 (2007), doi:[10.1529/biophysj.107.107474](https://doi.org/10.1529/biophysj.107.107474).
- [14] A. Hubert and R. Schäfer, *Magnetic domains: the analysis of magnetic microstructures* (Springer-Verlag, Berlin, Heidelberg, New-York, 1998).
- [15] R. P. Feynman, R. B. Leighton, and M. Sands, *The Feynman Lectures on Physics, Vol II* (Addison Wesley, 1964).
- [16] I. Jacobs and C. Bean, *Physical Review* **100**, 1060 (1955), doi:[10.1103/PhysRev.100.1060](https://doi.org/10.1103/PhysRev.100.1060).
- [17] FreeFEM++ (2007), URL <http://www.freefem.org/ff++/index.htm>.
- [18] M. Hanzlik, M. Winklhofer, and N. Petersen, *Earth and Planetary Science Letters* **145**, 125 (1996).
- [19] S. Dennis, S. Singh, and D. Ingham, *Journal of Fluid Mechanics* **101**, 257 (1980).
- [20] H. C. Berg, *Random Walks in Biology* (Princeton University Press, 1993).
- [21] L. C. Paoletti and R. P. Blakemore, *Current Microbiology* **17**, 339 (1988).
- [22] A. Witt, K. Fabian, and U. Bleil, *Earth and Planetary Science Letters* **233**, 311 (2005), doi:[10.1016/j.epsl.2005.01.043](https://doi.org/10.1016/j.epsl.2005.01.043).
- [23] I. S. M. Khalil, M. P. Pichel, L. Zondervan, L. Abelmann, and S. Misra, in *Experimental Robotics* (Springer Verlag, Bern, Switzerland, 2013), vol. 88 of *Springer Tracts in Advanced Robotics*, pp. 617–631.